**Fig. S1. Data quality directly impacts analysis outcomes.**

**(A)** MG apicobasal subregions/zones (1-to-5) display different signal levels and patterns, as shown by intensity profiles in **A'**. **(B)** MIP of an image in the acquired direction with intensity profile **B'** along a region of interest (dotted line) and transformed to look at it laterally **(C)** showing signal decay in the z-axis **C'**. **(D)** MIP of sub-optimal (1µm) vs optimal (0.19µm) z-steps E. (F-H) Artefacts, such as stripe artefacts, blurring, and inter-plane motion, were observed (representative images).
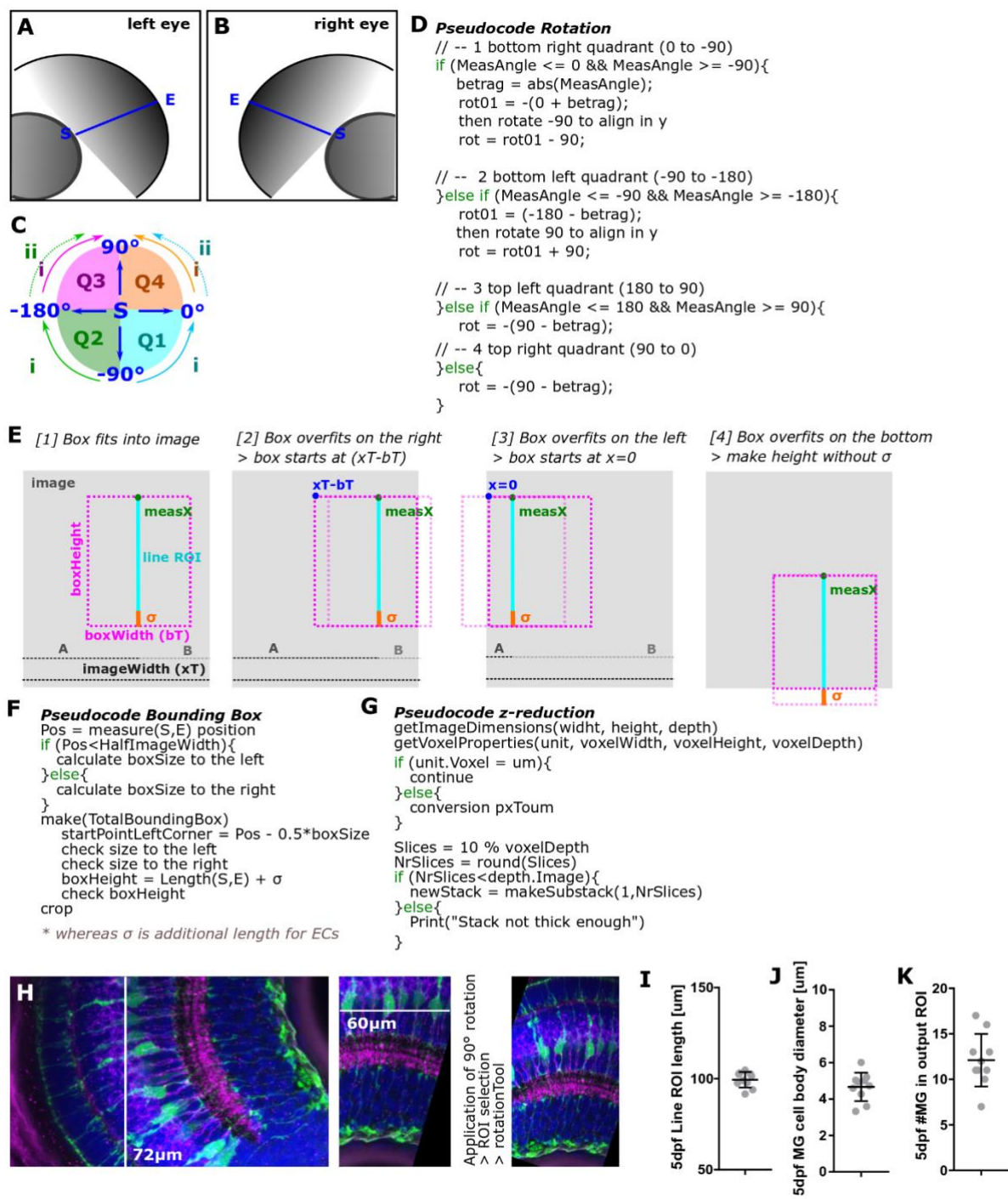
**A** left eye   **B** right eye

**C**

**D** *Pseudocode Rotation*

```
// -- 1 bottom right quadrant (0 to -90)
if (MeasAngle <= 0 && MeasAngle >= -90){
    betrag = abs(MeasAngle);
    rot01 = -(0 + betrag);
    then rotate -90 to align in y
    rot = rot01 - 90;

// --  2 bottom left quadrant (-90 to -180)
}else if (MeasAngle <= -90 && MeasAngle >= -180){
    rot01 = (-180 - betrag);
    then rotate 90 to align in y
    rot = rot01 + 90;

// -- 3 top left quadrant (180 to 90)
}else if (MeasAngle <= 180 && MeasAngle >= 90){
    rot = -(90 - betrag);
// -- 4 top right quadrant (90 to 0)
}else{
    rot = -(90 - betrag);
}
```

**E**  [1] Box fits into image   [2] Box overfits on the right > box starts at (xT-bT)   [3] Box overfits on the left > box starts at x=0   [4] Box overfits on the bottom > make height without σ

**F** *Pseudocode Bounding Box*

```
Pos = measure(S,E) position
if (Pos<HalfImageWidth){
    calculate boxSize to the left
}else{
    calculate boxSize to the right
}
make(TotalBoundingBox)
    startPointLeftCorner = Pos - 0.5*boxSize
    check size to the left
    check size to the right
    boxHeight = Length(S,E) + σ
    check boxHeight
crop

* whereas σ is additional length for ECs
```

**G** *Pseudocode z-reduction*

```
getImageDimensions(widht, height, depth)
getVoxelProperties(unit, voxelWidth, voxelHeight, voxelDepth)
if (unit.Voxel = um){
    continue
}else{
    conversion pxToum
}

Slices = 10 % voxelDepth
NrSlices = round(Slices)
if (NrSlices<depth.Image){
    newStack = makeSubstack(1,NrSlices)
}else{
    Print("Stack not thick enough")
}
```

**H**  72µm   60µm   Application of 90° rotation > ROI selection > rotationTool

**I** 5dpf Line ROI length [um]   **J** 5dpf MG cell body diameter [um]   **K** 5dpf #MG in output ROI

**Fig. S2. Semi-automatic ROI selection is critical for image comparability.**

**(A-B)** The workflow applies to the left and right eyes, which is computationally an inverse problem (S – start; E - end). **(C)** Rotation is performed in a multi-step fashion, depending on the original image position. **(D)** Pseudocode for image rotation. **(E)**

Bounding box starting points are determined based on the line ROI position. **(F)** Pseudocode for bounding box (x,y) establishment. **(G)** Pseudocode for z-reduction to establish stacks of the same depth. **(H)** For rectangular images, prior 90-degree rotation is suggested to avoid rotation-induced cropping. **(I)** The input line ROI determines the output image height, with the measurement of ROI length being an indicator for image similarity, such as an average 99.39 µm MG height at 120 hpf with a coefficient of variation (CoV) of 4.3% (n=10). To account for retinal curvature an additional section called sigma (default 10 µm) is appended. **(J)** Z-depth is reduced to a default 10 µm, as cell bodies are an average of 4.6 µm in diameter at 120 hpf (n=10; N=3 experimental repeats; mean ± s.d.). **(K)** The output image width is set to a default 60 µm to include on average 12 MG at 120 hpf (n=10; N=3 experimental repeats; mean ± s.d.).
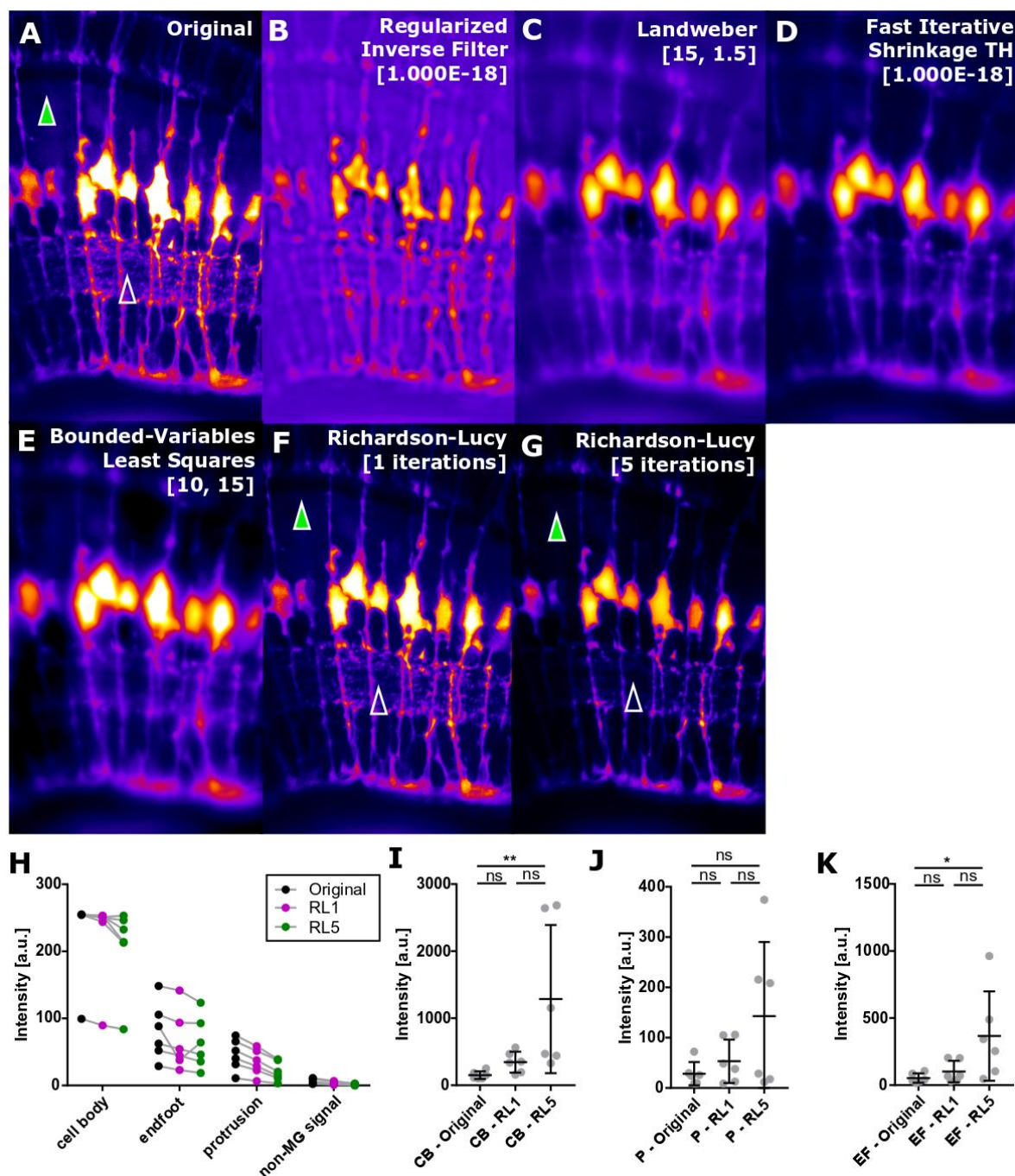
**Fig. S3. Confocal data PSF deconvolution increases contrast-to-noise ratio. (A)** Original image MIP (LUT Fire; green arrowhead – indicates non-MG background; unfilled arrowhead – MG IPL protrusions that could be lost with incorrect deconvolution). **(B)** Image after application of regularized inverse filter deconvolution. **(C)** Image after application of Landweber deconvolution. **(D)** Image after application of fast iterative shrinkage thresholding deconvolution. **(E)** Image after application of bounded least variables least-squares deconvolution. **F** Image after application of Richardson Lucy (RL) deconvolution with 1 iteration. **(G)** Image after application of RL

deconvolution with 5 iterations. **(H)** Image intensity measurements in MG cell bodies, endfeet, protrusions, and non-MG background signal (n=6 120 hpf; black – original, magenta – following deconvolution with RL 1 iteration, green - following deconvolution with RL 5 iterations). **(I)** CNR quantification in cell bodies (CB). **(J)** CNR quantification in protrusions (P). **(K)** CNR quantification in endfeet (EF; n=6 120 hpf; Kruskal-Wallis test; mean ± s.d.).
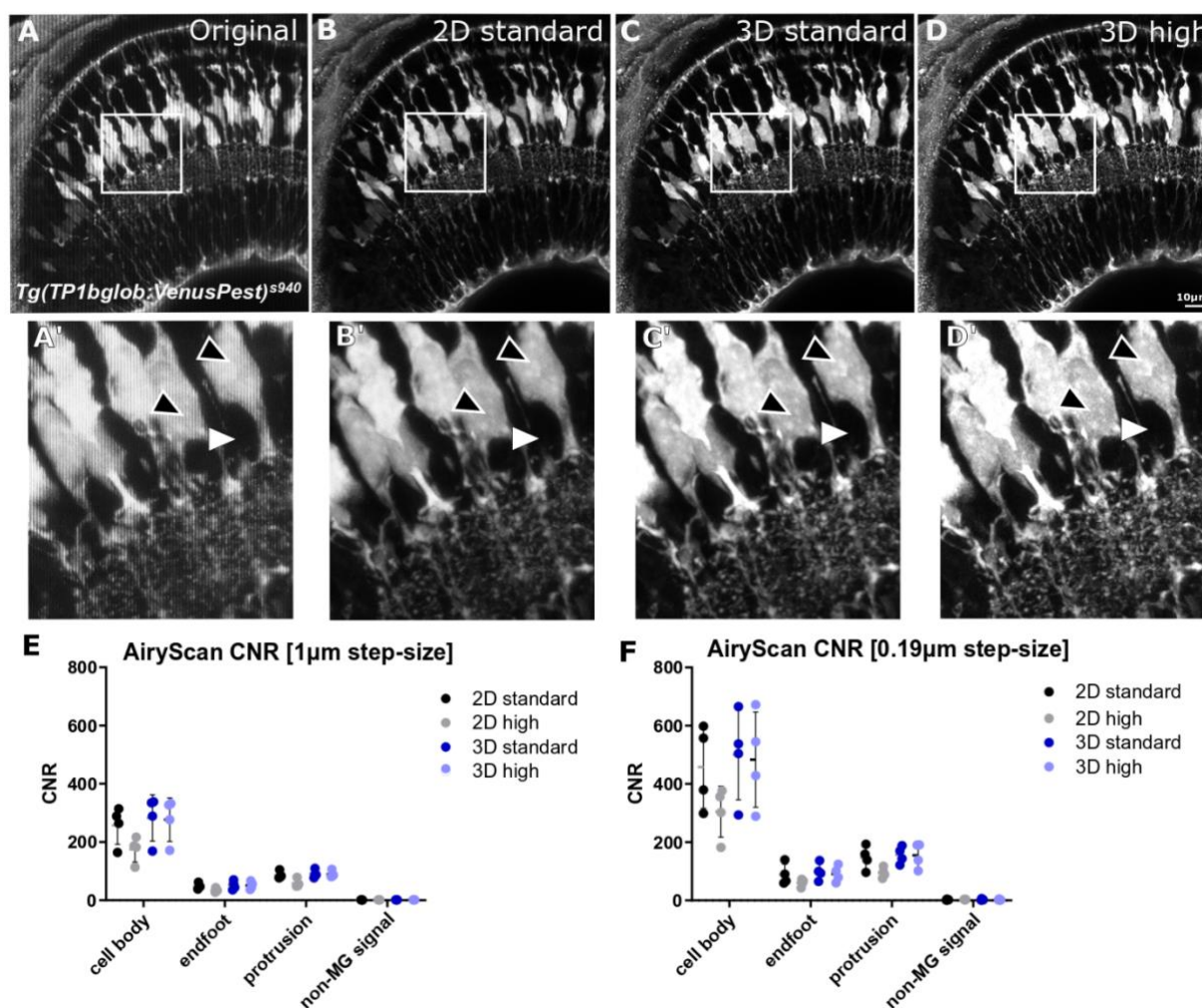
**Fig. S4. AiryScan processing increases contrast-to-noise ratio.**

**(A)** MIP of the original image without pre-processing. **(B)** MIP of an image after 2D standard AiryScan deconvolution. **(C)** MIP of an image after 3D standard AiryScan deconvolution, showing decreased background signal (white arrowhead). **(D)** MIP of an image after 3D high AiryScan deconvolution, showing increased structures noise/grains (black arrowheads). **(A'-D')** Insets of A-D, respectively. **(E-F)** CNR measurements in MG cell bodies, endfeet, protrusions, and non-MG signal, processed in 2D/3D, standard/high, acquired with 1µm (E) and 0.19µm (F) z-stack step sizes (n=4 120 hpf; mean ± s.d.).
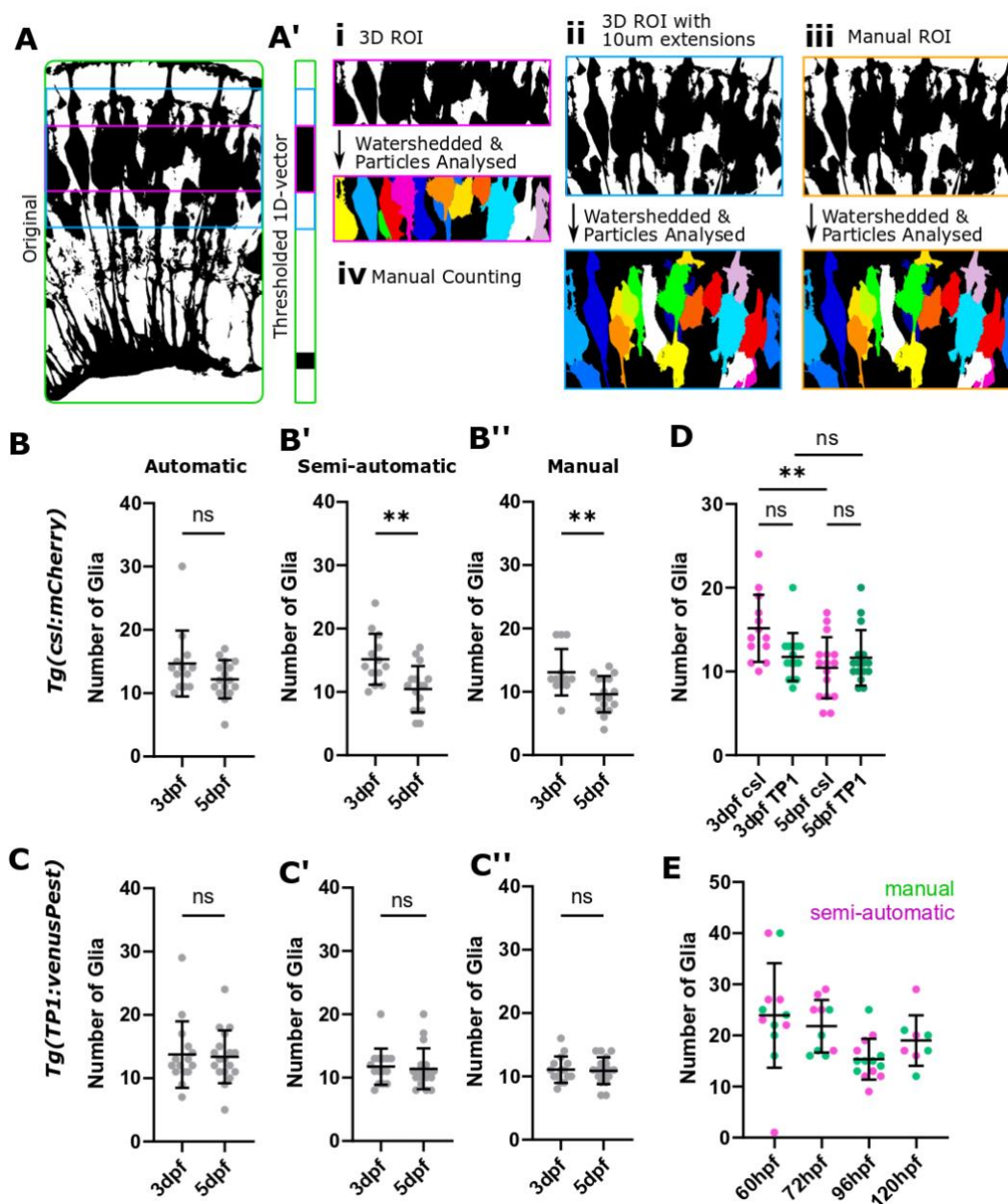
**Fig. S5. Cell number counts are influenced by the visualization technique used.**
**(A)** Segmented 3D stacks were used to quantify the number of cells. **(A')** To
automatically extract the retinal layer containing MG cell bodies, the ZonationTool was
applied and then segmented (i). (ii) To allow for errors, the ROI from (i) was extended by
10μm in both directions. (iii) Alternatively, a semi-automatic approach was used, using
one manually drawn ROI for each group. (iv) To compare measurements from

the above, manual counting was used as standard. **(B)** Comparison of measurement outcomes in *Tg(csl:mCherry)* (B p=0.0027, B' p=0.0027, B'' p = 0.0083; 3dpf n=13, 5dpf n=16; N=2; unpaired two-tailed Students' t-test; mean ± s.d.). **(C)** Comparison of measurement outcomes in *Tg(TP1:venusPest)*. Semi-automatic and manual measurements were more sensitive than fully automated analysis. Cell number is decreased from 72-to-120 hpf in *Tg(csl:mCherry)* but not *Tg(TP1:venusPest)* (C p=0.8347, C' p=0.7500, C'' p=0.8103; 72 hpf n=13, 120 hpf n=16; N=2; unpaired two-tailed Students' t-test; mean ± s.d.). **(D)** Comparison of the glia number of both transgenics using semi-automatic measurements (mean ± s.d.). **(E)** Comparison of cell number measurements from 60-to-120hpf using semi-automatic and manual measurements (mean ± s.d.).
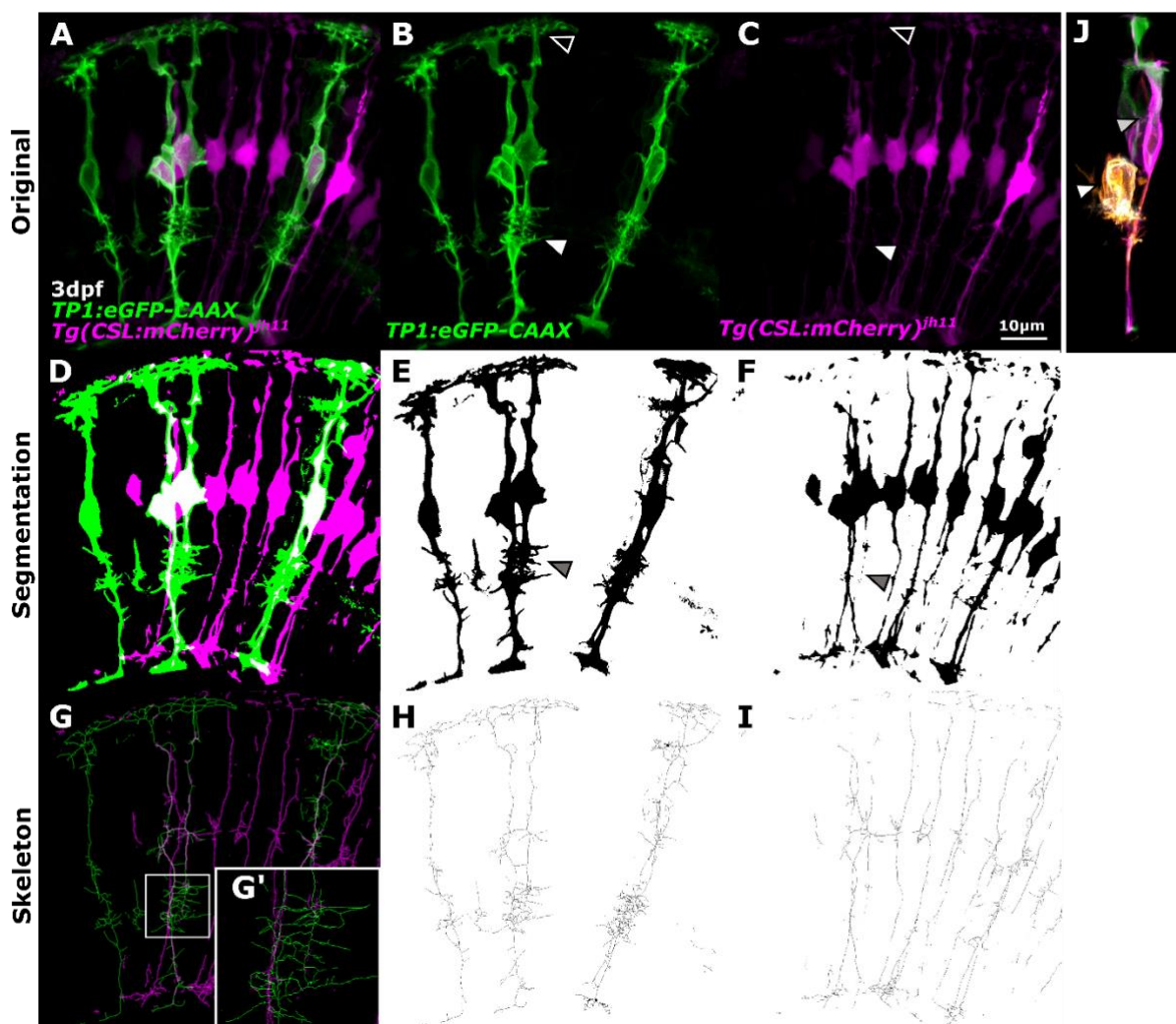
**Fig. S6. MG membrane and cytosol segmentation show membrane signals to deliver better segmentation results.**

**(A-C)** MG cytosolic transgenic (magenta) with a mosaic expression of MG membrane marker (green). **(D-F)** Segmentation of membrane and cytosol markers. **(G-I)** Skeletonization of the segmented images. **(J)** Cell labelling can result in an unspecific signal, as seen by an individual MG (grey arrowhead) and amacrine cell (white arrowhead) being labelled.
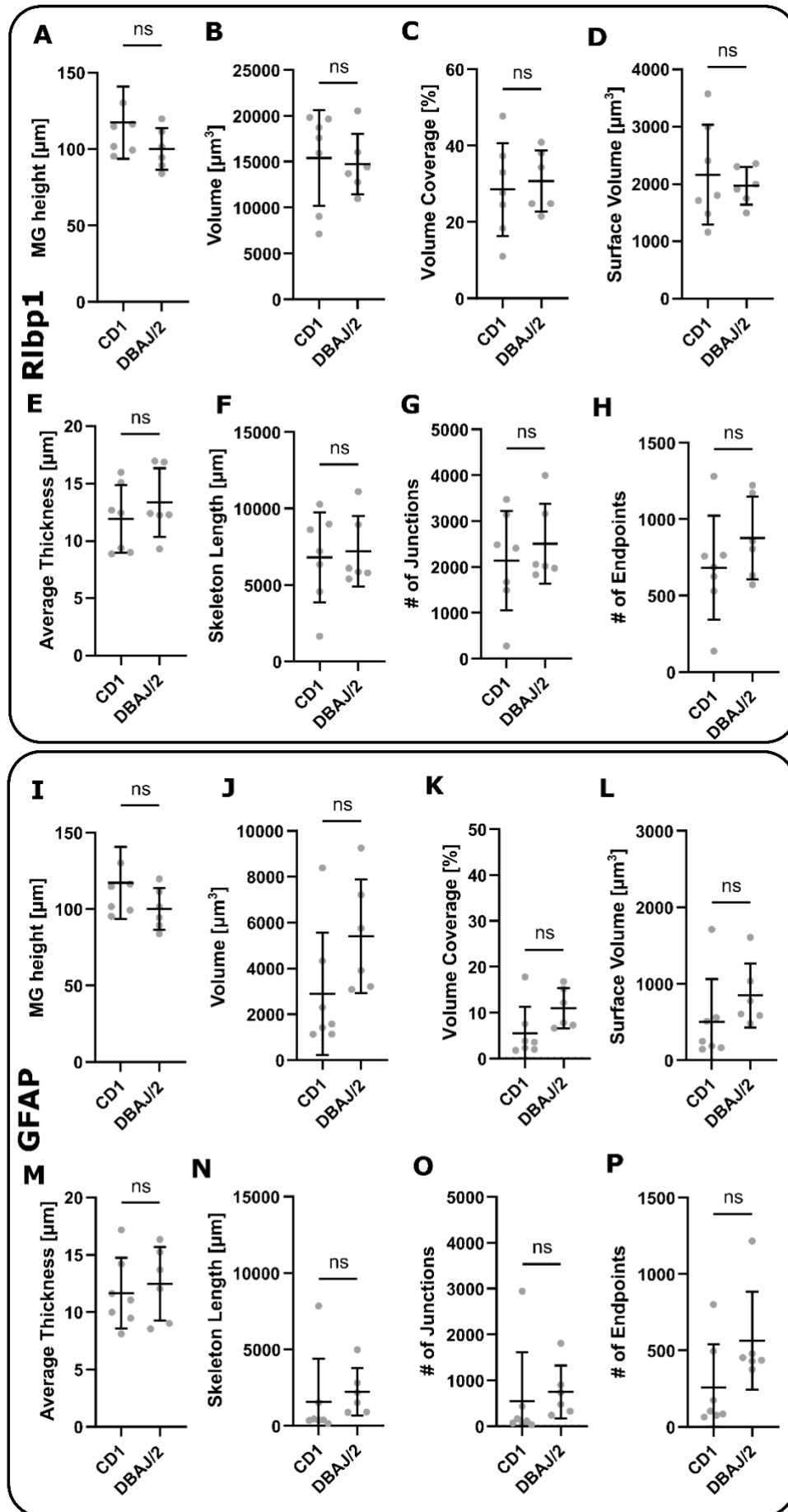
**Fig. S7. Mouse glaucoma model quantification using the GliaMorph toolkit. (A-H)**
Quantification of Rlbp1 data showed no statistically significant difference
between CD1 controls and DBA/J2 (n=7 stacks from 3 mice each; MG height
p=0.1375; Volume p=0.7308; Volume coverage p=0.6282; Surface volume p>0.9999;
Average thickness p=0.6282; Skeleton length p=0.9452; Number of junctions
p=0.6282; Number of endpoints p=0.2949; Mann-Whitney test). **(I-P)** Quantification of
GFAP data showed no statistically significant difference between CD1 controls and
DBA/J2 (n=7 stacks from 3 mice each; MG height p=0.1375; Volume p=0.0734;
Volume coverage p=0.0734; Surface volume p=0.0734; Average thickness p=0.7308;
Skeleton length p=0.0734; Number of junctions p=0.0734; Number of endpoints
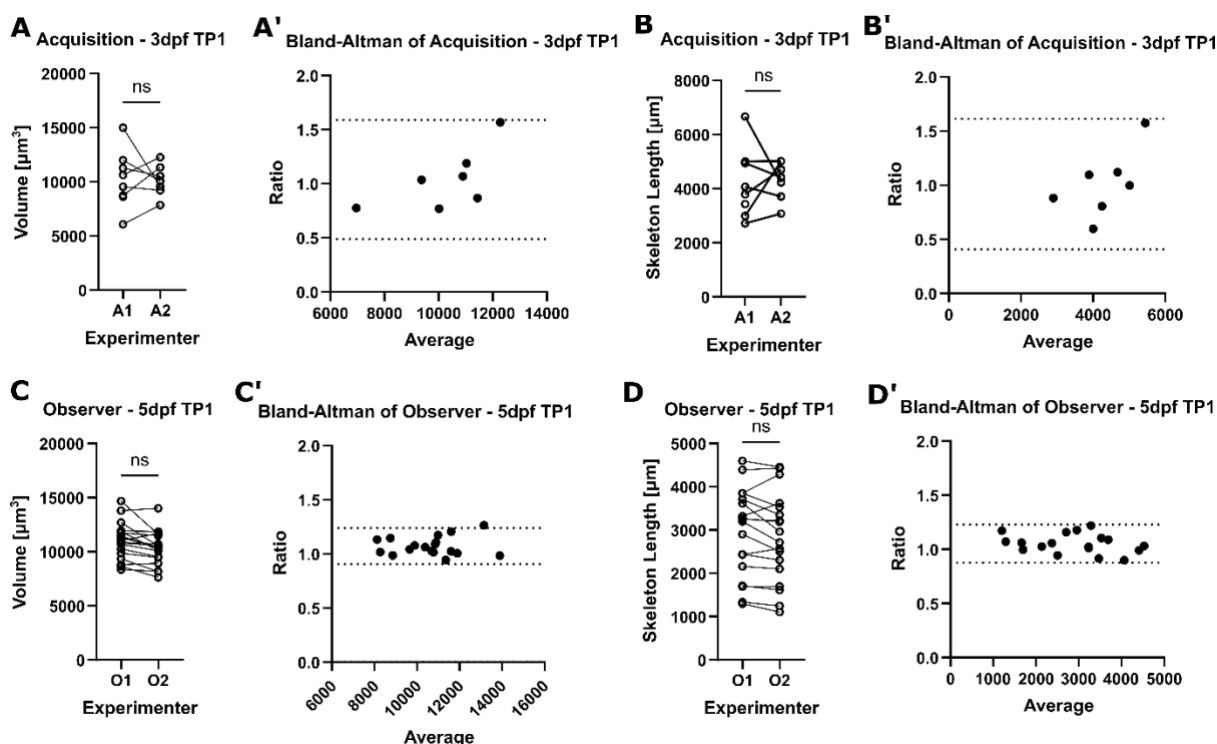p=0.1375; Mann-Whitney test).

**Fig. S8. GliaMorph is highly robust, as shown by inter-observer analysis.**

**(A, A')** Comparing the analysis outcomes using MG volume from data acquired by two different people showed no statistically significant difference (p=0.9211 unpaired t-test) and no bias measured by the Bland-Altman ratio (1.039). **(B, B')** Comparing the analysis outcomes using skeleton length from data acquired by two different people showed no statistically significant difference (p= 0.8460) unpaired t-test) and no bias was measured by the Bland-Altman ratio (1.010; n=8; N=1). **(C, C')** Comparing the analysis outcomes using MG volume analysed independently by two people showed no significant difference (p=0.1934 unpaired t-test) and no bias measured by Bland-Altman ratio (1.073). **(D, D')** Comparing the analysis outcomes using MG skeleton length analysed independently by two people showed no significant difference (p= 0.7363 unpaired t-test) and no bias measured by Bland-Altman ratio (1.053; n=18; N=2).